Journal of Materials Chemistry A

Accepted Manuscript

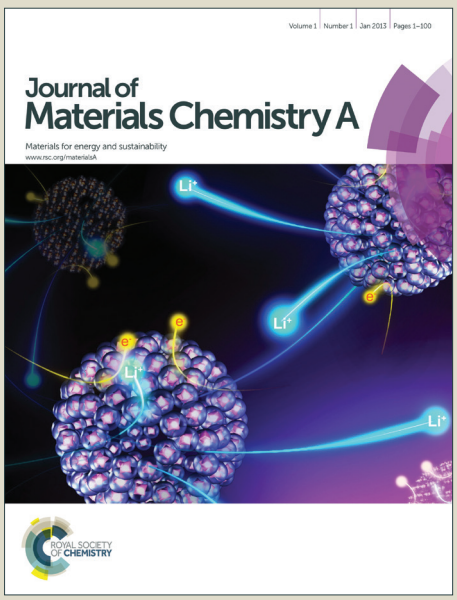

ROYAL SOCIETY OF CHEMISTRY

www.rsc.org/materialsA

Journal of Materials Chemistry A RSCPublishing

ARTICLE

Understanding the stepwise capacity-increase of high energy low-Co Li-rich cathode materials for lithium ion batteries

Cite this: DOI: 10.1039/x0xx00000x

Received 00th January 2014,
Accepted 00th January 2014

DOI: 10.1039/x0xx00000x

www.rsc.org/

Delai Ye,[a] Bei Wang,[a] Yu Chen,[a] Guang Han,[b] Zhi Zhang,[b] Denisa Hulicova-Jurcakova,[a] Jin Zou,[b,c] Lianzhou Wang[a]*

Li-rich layered materials as a promising high-energy cathode candidate have attracted much attention in recent years for next generation lithium ion batteries. However, the fundamental mechanism of the high specific capacity in these cathode materials has not been fully revealed so far. In this work, we report a new class of Li-rich cathode materials $Li[Co_xLi_{1/3-x/3}Mn_{2/3-2x/3}]O_2$ (x=0.087, 0.1, 0.118) with a very low level of Co doping, which exhibit impressive stepwise capacity increase over dozens of cycles from less than 50 mAh g^{-1} to around 250 mAh g^{-1}. A systematic study on their composition, crystal structure and electrochemical performance revealed that the small change of Co content has negligible effect to the crystal structure and morphology, but plays an important role in enhancing the activation rate of the Li_2MnO_3 phase. In addition, optimized cycling potential window and current rate were proven to be critically important for effective Li_2MnO_3 activation and better long-term cycling stability.

Introduction

Lithium ion batteries (LIBs) have become the dominant power source for portable electronics in recent years due to their high energy densities.[1, 2] The massive consumption of fossil fuels and the corresponding derived environment problems have triggered the rapid development of electric vehicles, which are highly dependent on large-scale applications of high performance LIBs.[3] Currently, a large number of new anode materials have been developed with concurrent superior high specific capacity of up to 1000 mAh g^{-1} and good power density;[4-7] however, the specific capacities of the major cathode materials such as $LiCoO_2$, $LiFePO_4$ and $LiMn_2O_4$ are still too low (less than 170 mAh g^{-1}) to match the anode side.[8] Therefore, searching new cathode materials with high capacity is critical for the future development of LIBs and even the electric vehicle industry.

Li-rich Mn-based layered compounds are a new series of high energy cathode materials that have attracted significant recent attention. Generally, they are composed of two highly integrated layered phases and can be formulated as $xLi_2MnO_3\cdot(1-x)LiMO_2$ (0 <x <1, M = Mn, Co, Ni or their mixture).[9, 10] Typically, the Li-rich Li_2MnO_3 phase can be activated at a high charging voltage above 4.5 V. During the activation process, the oxygen ions of the crystal lattice will be extracted in the form of oxygen with concurrent deintercalation of Li^+ from the transition metal (TM) layers and diffusion of TM ions to the Li layers. The activation of Li_2MnO_3 phase has been demonstrated to provide extra specific capacity to the Li-rich cathode materials, which might deliver a specific capacity of over 250 mAh g^{-1} at room temperature.[11, 12] However, there are still a few serious challenging issues that the Li-rich cathode materials have to address before practical application including the low initial columbic efficiency, poor cycling stability, low rate capability and long term working voltage decline.[13] To solve these problems, it is essential to fundamentally understand the lithium storage mechanisms and the origin of these problems from the aspects of chemical composition and crystal structure.[14] Most Li-rich cathode materials in the Li-Mn-Co-O system have been reported with a Co/Mn mole ratio equal or more than 1/3 while the materials with a Co/Mn ratio less than 1/3 are rarely investigated.[15-17] In fact, it would be of advantage if the Co content in Li-rich cathode materials can be significantly reduced due to the high cost and toxicity of Co. In this regard, we have studied a series of Li-rich Co-doped materials recently with a further reduced Co/Mn mole ratios down to 1/6 and a variable ratios of Li/(Mn+Co).[18, 19] It was found that the specific capacities of these materials increased upon cycling in the first cycles and such a small amount of Co doping can effectively promote the Li_2MnO_3 activation.

In this work, we report a systematic study on a new class of low-Co Li-rich layered cathode materials $Li[Co_xLi_{1/3-x/3}Mn_{2/3-2x/3}]O_2$ (x=0.087, 0.1, 0.118) which exhibit remarkable capacity increase in the first dozens of cycles. This unique phenomenon of stepwise capacity increase was revealed to be associated with gradual activation of the Li-rich Li_2MnO_3 phase, which is highly dependent on a few key parameters including the cycling potential window, the amount of Co doping and the cycling current rate. The morphology, crystal structure and electrochemical performance of these materials were also investigated in details. This work will not only help to understand the origin of the superior high specific capacity of Li-rich

cathode materials, but also shed light on the design of cost-effective and scalable high performance cathode materials for LIBs.

Experimental section

Materials synthesis

All the chemicals are purchased from Aldrich Sigma. The $Li[Co_xLi_{1/3-x/3}Mn_{2/3-2x/3}]O_2$ (x=0, 0.087, 0.1, 0.118) composites were synthesized by two steps. Firstly, stoichiometric amount of $Mn(NO_3)_2$ $4H_2O$ and $Co(NO_3)_2{\cdot}6H_2O$ were dissolved in distilled water and then slowly dropped to equal volume of 0.2 M sodium carbonate solution under vigorous stirring. After 20 h aging at room temperature, the metal ions were fully co-precipitated as carbonates. In the second step, the collected carbonates were pre-treated at 500 °C for 5 h in air and then calcined with stoichiometric amount of $LiOH{\cdot}H_2O$ at 900 °C for another 12 h in air to produce the final cathode materials. A 3 wt % excess of $LiOH{\cdot}H_2O$ was applied for the calcination process to compensate for Li volatilization at elevated temperature.

Structural and morphological characterization

The composition of each sample was determined by a Varian 725-ES Inductively Coupled Plasma Atomic Emission Spectroscopy (ICP-AES). X-ray diffraction (XRD) was conducted on a Bruker Advanced X-Ray Diffractometer (40 kV, 30 mA) with Cu Kα (λ=0.15406 nm) radiation to detect crystalline structures of the powder samples and electrodes at a scanning rate of 1^o min^{-1}. X-ray photoelectron spectrometry (XPS) analysis was performed by a Kratos Axis Ultra X-ray Photoelectron Spectrometer using $Al_{K\alpha}$ (1253.6 eV) X-ray. Field-emission scanning electron microscopy (SEM, JEOL 7800) and transmission electron microscopy (TEM, Philips FEI Tecnai F20 operated at 200 kV) were applied to collect the morphological and local structure information of the samples.

Electrochemical measurement

All the electrochemical measurements of the materials were conducted on CR2032 coin cells. The working electrodes were prepared by doctor-blade method to coat slurries containing 70 wt % of the active materials, 20 wt % of acetylene black and 10 wt% of polyvinylidene fluoride (dissolved in N-methyl-2-pyrrolidone with a concentration of 5 wt %) onto aluminum foils (0.7 cm^2). After drying under vacuum at 120° C for 12 h, these working electrodes were then assembled into coin cells in an argon-filled glove box with lithium foil as the negative electrode and 1 M $LiPF_6$ in a mixture of ethylene carbonate (EC) and dimethyl carbonate (DMC) (1:1) as the electrolyte. Galvanostatic charge/discharge test was performed on a multi-channel Land CT2001A battery testing system. Cyclic voltammetry (CV) measurements were conducted on a CHI660E electrochemistry workstation at a scan rate of 0.2 mV s^{-1} between 2-4.8 V. The electrochemical impedance spectroscopy (EIS) was tested on the same electrochemistry workstation at open-circuit voltage between 100 kHz and 10 mHz. All the electrochemical tests were performed at room temperature.

Results and discussion

The compositions of all the Co-doped samples are confirmed by ICP-AES analysis as shown in **Table 1**. Both the Mn/Co and Li/(Mn+Co) ratios are in good agreement to the nominal values.

Table 1. ICP-AES analysis results of the $Li[Co_xLi_{1/3-x/3}Mn_{2/3-2x/3}]O_2$ (x=0.087, 0.1, 0.118) composites.

	Mn:Co		Li : (Mn+Co)	
x	Nomina	Experimenta	Nomina	Experimenta
0.08	7	6.88	1.87	1.92
0.1	6	5.89	1.86	1.88
0.11	5	4.96	1.83	1.81

XRD patterns of all the powder samples are displayed in **Figure 1a**. All major diffraction peaks can be well indexed to the R-3m space group (JCPDS No. 84-1634) as a typical layered phase, and some minor peaks between 20° and 25° are due to the localized $LiMn_6$ superlattice that belongs to the monoclinic Li_2MnO_3-like phase.[20-22] It is worth noting that a higher (003) peak can be observed over the (104) peak in each sample. This indicates a low degree of transition metals (TM) existed in the Li layers, which is also supported by the well split pairs of (006)/(012) and (018)/(110) peaks.[23] All the samples exhibit sharp diffraction peaks, especially the two main peaks of (003) and (114) which have apparently narrow full-width at half maximum (FWHM) of around 0.12° and 0.23°, respectively, indicating a high degree of crystallinity for the samples (**Table 2**). In addition, the diffraction peaks are highly identical among these materials, suggesting that a small amount of Co-doping does not change the crystal structure or cause impurity phases. However, taking a careful look at the enlarged (003) main diffraction peak in **Figure 1b**, it can be found that this peak actually shifts slightly to a higher angle with the increase of Co amount (18.645° for the x=0 sample, and 18.704° for the x=0.118 sample). Such a gradual increase of the diffraction peak position indicates the decrease of lattice parameter, which can be well explained by the smaller ionic size of Co^{3+} (0.545 Å) as guest species than the ionic size of Mn^{4+} (0.53 Å) and Li^+ (0.76 Å), indicating the homogeneous distribution of the Co doping in the whole crystal structure.[15, 16]

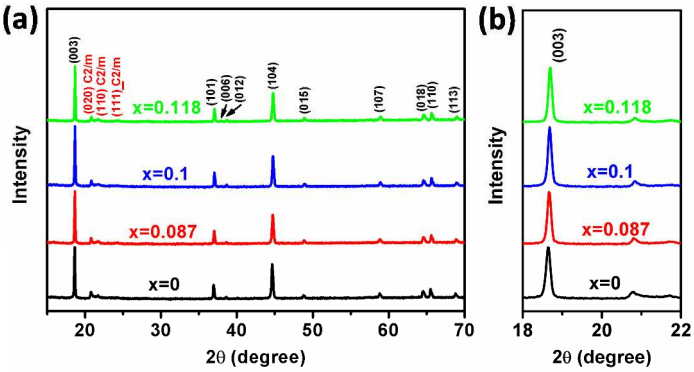

Figure 1. (a) Powder XRD patterns of the original $Li[Co_xLi_{1/3-x/3}Mn_{2/3-2x/3}]O_2$ (x=0, 0.087, 0.1, 0.118) compounds; and their enlargement between 20° and 25°.

Table 2. Full-width at half maximum (FWHM) of the typical XRD diffraction peaks of the $Li[Co_xLi_{1/3-x/3}Mn_{2/3-2x/3}]O_2$ (x=0.087, 0.1, 0.118) composites.

	FWHM	
x	(003)	(104)
0	0.136°	0.226°
0.087	0.119°	0.235°
0.1	0.117°	0.225°
0.118	0.109°	0.233°

Figure 2 presents the SEM images of the samples. Basically, 2-3 μm sized microspheres can be found in each sample. From the high-magnification SEM images of the typical x=0.087 and x=0.1 samples (**Fig. 2e and 2f**), it is clearly revealed that these microspheres are composed of nano-sized sub-units to form aggregated hierarchical structure. This microstructure could be advantageous for the cathode materials in two aspects. The primary nanoparticles might provide short Li^+ diffusion channels and concurrently increase the surface area for the electrode-electrolyte contact;[24, 25] The lattice strain and volume change of the materials during long term Li^+ intercalation/deintercalation may be effectively accommodated by the porous aggregate structure.

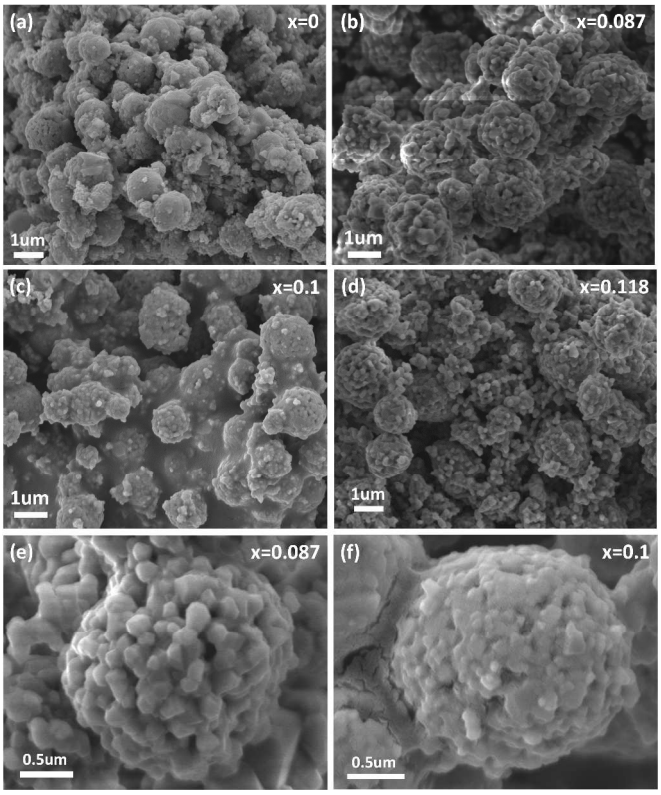

Figure 2. (a) to (d) SEM images of the $Li[Co_xLi_{1/3-x/3}Mn_{2/3-2x/3}]O_2$ (x=0, 0.087, 0.1, 0.118) compounds; (e) and (f) high-resolution SEM images of the typical x=0.087 and 0.1 samples.

TEM images and selected area electron diffraction (SAED) patterns revealed similar morphologies and crystalline structure in all the samples. Note that because of the large particle size as revealed by SEM in Fig. 2, it's difficult for the electron beam to passing through the particle; as a result, most parts of the particle image are in dark in TEM images. Nevertheless, the nano-scale smaller secondary nanoparticles around the large spherical particle edges can be seen (**Figure 3a, 3b)** for the typical x=0.087 sample. Additionally, HRTEM images of a selected primary nanoparticle domain oriented along $[1\text{-}10]_{mon}$ and $[010]_{mon}$ clearly reveal the perfect layered structure along the [001] zone axis.[12] Sharp and bright SAED patterns were also acquired along the corresponding directions. Both patterns point to a high crystallized layered structure; however, the SAED pattern along the $[1\text{-}10]_{mon}$ presents diffuse streaks besides the sharp and bright spot reflections. These streaks are characteristic of the monoclinic structure and can be well explained by the random overlap of well α–sublattice ordered TM layers along the c-axis, further confirming the existence of monoclinic unit cells.[12, 26, 27]

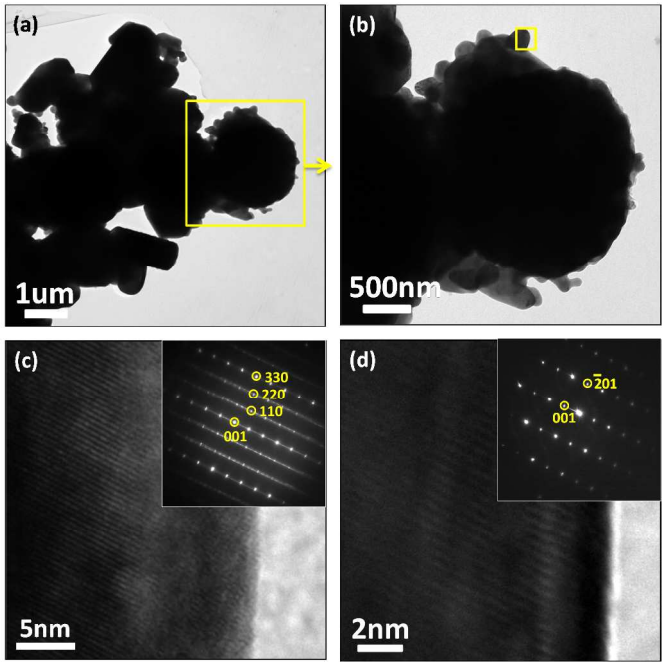

Figure 3. (a) TEM images of the x=0.087 sample; (b) Enlargement of the yellow frame in (a); (c, d) HRTEM images of the yellow frame area in (b) along two different zone axis of $[1\text{-}10]_{mon}$ and $[010]_{mon}$. Right-top inset images in (c) and (d) are the corresponding SAED patterns.

XPS of Mn 2p and Co 2p of the Co-doped pristine materials are shown in **Figure 4**. It can be found that the binding energies of both the Mn and Co are very similar in these samples, implying that Mn and Co keep a stable valence state in our samples when the Mn/Co is slightly changed. Specifically, for the Mn $2p_{3/2}$ and $2p_{1/2}$, the binding energies are about 642.1 eV and 653.6 eV, respectively, with an energy split of 11.5 eV. This is highly consistent with those reported of Mn^{4+}, indicating the valence of Mn in these composites is mainly 4+.[28, 29] On the other side, the spectrum of Co appears almost the same as the reported $LiCoO_2$,[30] suggesting the 3+ oxidation state of Co in our samples.

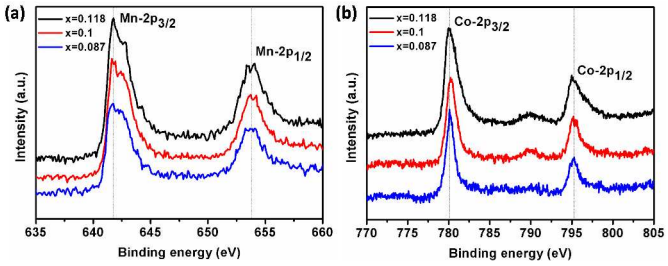

Figure 4. XPS patterns of (a) Mn and (b) Co elements in the $Li[Co_xLi_{1/3-x/3}Mn_{2/3-2x/3}]O_2$ (x=0.087, 0.1, 0.118) compounds.

The cycling performance of the $Li[Co_xLi_{1/3-x/3}Mn_{2/3-2x/3}]O_2$ (x=0, 0.087, 0.1, 0.118) composites at the first 120 charging-discharging cycles at three potential windows of 2-4.6 V, 2-4.8 V and 2-5 V is shown in **Figure 5**. It is interesting to find that the specific discharge capacities of these samples are increased upon cycles, and such an increase is particularly prominent at 2-4.8 V and 2-5 V. This phenomenon is different from the general capacity decay in traditional cathode materials during cycling and can be attributed to the continuous activation of the Li_2MnO_3 phase. This continuous activation phenomenon has been proposed to be promoted by Co doping, which can remarkably decrease the energy barrier of the oxygen extraction from the crystal lattice.[18, 19] The effect of Co doping can be further supported here by the fact that all the Co-doped samples deliver a much higher capacity than the pure Li_2MnO_3 sample over cycles, particularly at 2-4.8 V and 2-5 V, and a slight change of the Co content can make a significant difference to the electrochemical performances of these materials. For example, the discharge capacities of the x=0.118, x=0.1 and x=0.087 samples after 120 cycles at 2-4.8 V are 213 mAh g^{-1}, 223 mAh g^{-1} and 234 mAh g^{-1}, respectively, while it is only 50 mAh g^{-1} for the pure Li_2MnO_3 sample at the same condition.

Note that the capacity increase is also highly related to the cycling voltage range. For each sample, it is apparent that the higher the upper cut-off voltage, the faster the capacity increases. As the Li_2MnO_3 activation process involves a high potential O_2-release reaction, a higher cut-off potential is supposed to facilitate deeper Li_2MnO_3 activation and Li extraction, thus leading to the faster capacity increase.[31, 32] However, it is also found that the long term cycling stability of these Co-doped samples was poor at 2-5 V, where the discharge capacities climbed to the peak value in only a few cycles and then declined quickly. In contrast, the discharge capacities of these samples took more cycles to maximize but then kept stable in the consequent cycles at 2-4.8 V. Such a poor cycling stability at 2-5 V could be ascribed to the instability of the electrolyte and possible side reactions of the samples on the electrode-electrolyte interface at high potential.[33] Therefore, 2-4.8 V is used in the following work as an optimized voltage range to effectively activate the Li_2MnO_3 phase of the samples and concurrently maintain good long term cycling stability.

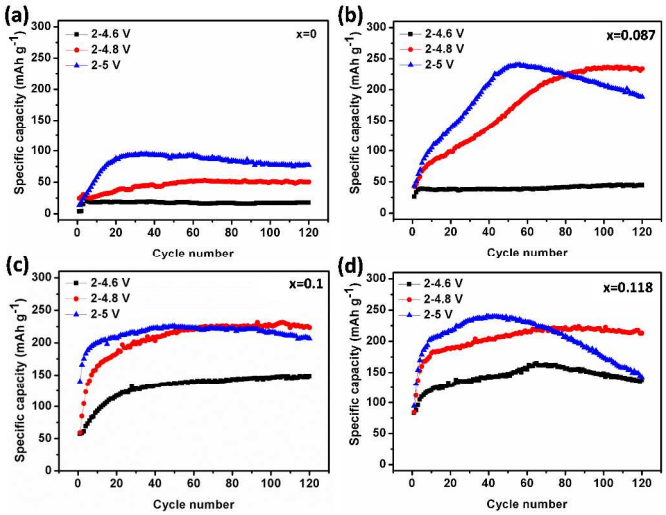

Figure 5. Specific discharge capacities of the $Li[Co_xLi_{1/3-x/3}Mn_{2/3-2x/3}]O_2$ (x=0, 0.087, 0.1, 0.118) composites in the first 120 charging-discharging cycles at three potential windows of 2-4.6 V, 2-4.8 V and 2-5 V. The current density is 30 mA g^{-1}.

To further explore the effect of Co doping to the electrochemical performance, the specific discharge capacities of all samples in the first 120 cycles at 2-4.8 V are compared in **Figure S1**. It can be found that the capacity rapidly increased upon cycles in the Co-doped samples while the Li_2MnO_3 sample, although increased as well, maintained a low capacity of less than 50 mAh g^{-1}. In addition, as the content of Co grows, the capacity increases faster in the first a few cycles, suggesting that Co can facilitate the capacity increase. This is further supported by the cycling performance of the x=0.143 and 0.182 samples under the same testing condition (**Figure S2**). With higher Co/Mn mole ratios of 4 and 3, the activation of the Li_2MnO_3 was completed much faster, as a result, the capacity of these two samples increased for only 2 and 4 cycles, respectively and then gradually decreased. On the other side, it is noted that the x=0.087 sample delivered the highest peak capacity of 234 mAh g^{-1} after 120 cycles while the x=0.118 sample achieved the smallest of 213 mAh g^{-1}. This is probably because the increase of Co is at the cost of the Li_2MnO_3 phase, which is the main contributor to the fully activated capacity. On the other side, it can be found from **Figure 6** that the columbic efficiencies of the sample at 2-4.8 V potential window are similar in the first 120 cycles. In the first 4 or 5 cycles, all of them exhibited quite low columbic efficiency. After the initial 4 or 5 cycles, the efficiency increased quickly from around 60% in the first cycle to over 95% and then became stabilized for the following cycles. This indicates that all these samples experienced the capacity loss mainly in the first 4 or 5 cycles, but retained the extra capacity in the following cycles with negligible electrolyte decomposition during the relatively mild activation process.

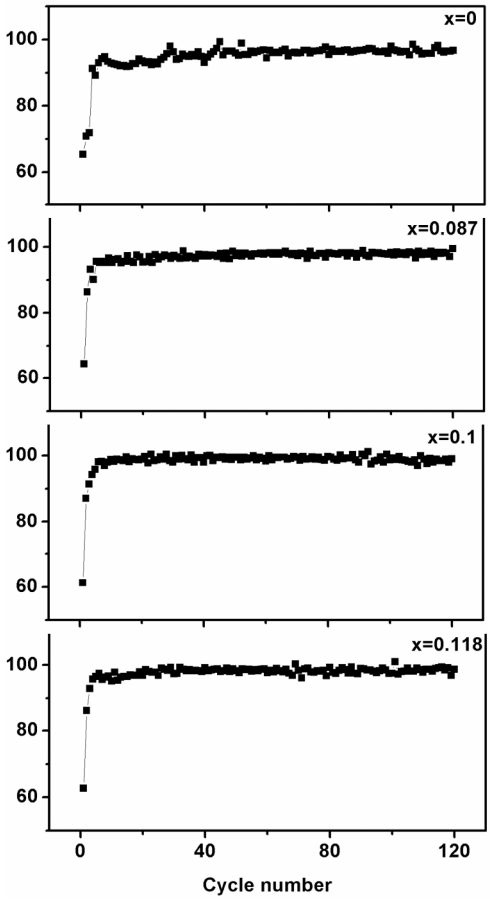

Figure 6. Columbic efficiencies of the $Li[Co_xLi_{1/3-x/3}Mn_{2/3-2x/3}]O_2$ (x=0, 0.087, 0.1, 0.118) composites between 2-4.8 V potential window in the first 120 charging-discharging cycles.

Detailed charging-discharging curves of each sample are presented in **Figure 7**. For the first charge, a short plateau between 4 V and 4.5 V appeared in all Co-doped samples. This can be ascribed to the oxidation of Co^{3+} to Co^{4+}.[19, 34] More importantly, a long first charge plateau above 4.5 V was developed in the Co-doped samples and grew longer as the Co content increased. This plateau is associated with the Li_2MnO_3 activation process, which involves a few sub-reactions including a further Li extraction from the TM layers, TM rearrangement and O_2 generation from the crystal structure.[9, 11, 35] Therefore, it can be deduced that a slightly higher content of Co-doping can effectively promote the Li_2MnO_3 activation from the very beginning. Compared with the Li_2MnO_3 sample, another impressive feature in the Co-doped samples is the evolution of the 3 V discharge plateau which was invisible in the first discharge but dominated the discharge curve after just a few cycles. This plateau is well accepted to be from a newly formed defect spinel phase embedded on the parent layered structure.[18, 36, 37]

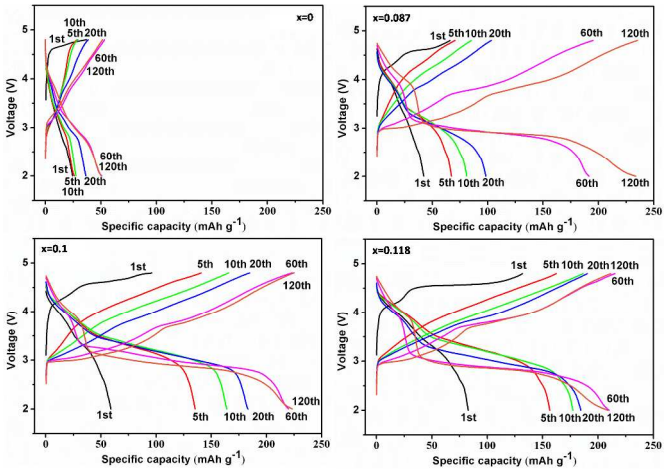

Figure 7. Charging-discharging curves of the $Li[Co_xLi_{1/3-x/3}Mn_{2/3-2x/3}]O_2$ (x=0, 0.087, 0.1, 0.118) composites at different cycles between 2-4.8 V potential window.

CV measurements were also conducted to further understand the redox reactions of the Co-doped materials upon cycling and the CV curves in the first 10 cycles at 2-4.8 V and a scan rate of 0.2 mV s^{-1} are shown in **Figure 8**. In general, a sharp and high oxidation peak at around 4.6 V appeared in the first charge and then faded in the second charge and almost disappeared after 5 cycles. This feature is well consistent with the behavior of the charge plateau above 4.6 V as shown in **Figure 7**, suggesting majority of the Li_2MnO_3 phase was activated in the first few cycles. In addition, a pair of redox peaks centered at around 3.2 V was gradually developed in all samples and became the largest after 10 cycles. Such a pair of peaks can be ascribed to the redox reaction of the Mn^{3+}/Mn^{4+} in a spinel environment, suggesting that the layered structure of these Co-doped materials was gradually transformed to a new spinel phase during cycling.[38] As the Co content increased, it is noted that a pair of 4.1 V redox peaks was also enlarged, which can be ascribed to the Co^{3+}/Co^{4+} redox pair,[19] indicating more Co involved in the electrochemical reactions. In addition, it can be clearly seen that the area of the CV loops, which is proportional to the charge/discharge capacity, was growing obviously upon cycles in each sample; on the other hand, the CV loops expanded apparently faster in the sample with higher Co content. All these features are well consistent with the above cycling results in **Figure 6**, further supporting the fact that the capacities of the samples gradually increase upon cycling and a slight increase of Co in the samples can drastically facilitate the capacity increment.

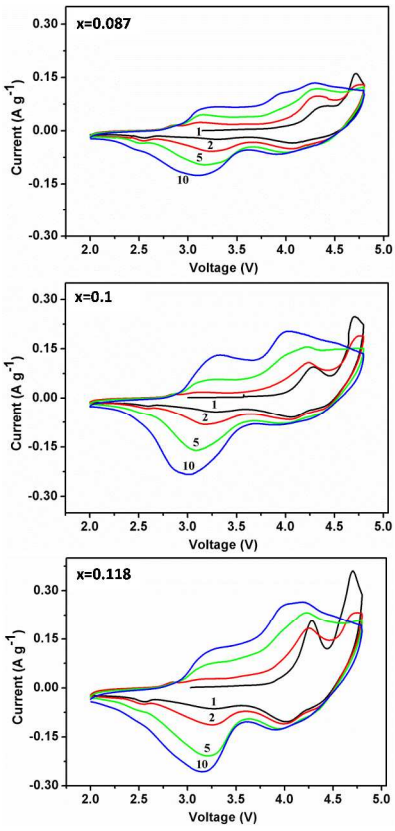

Figure 8. CV curves of the $Li[Co_xLi_{1/3-x/3}Mn_{2/3-2x/3}]O_2$ (x=0.087, 0.1, 0.118) composites at 2-4.8 V in the first 10 charging-discharging cycles.

The cycling performance of the Co-doped samples was also compared at different current rates of 0.1 C, 0.2 C and 0.5 C and the results of the first 120 cycles are shown in **Figure 9**. It is obvious that the capacity-increase was remarkably retarded at 0.2 C and almost vanished at 0.5 C. Considering the complex structure arrangement and diffusion of the heavy transition metals and oxygen ions during the Li_2MnO_3 activation process, a poor kinetics could be expected to account for such a small capacity increase at high rates.[39] On the other side, it can be found that the capacity-increase at 0.2 C also follows the trend that the more the Co doping, the faster the capacity increases. It has been reported that the Li_2MnO_3 had very poor rate capability while the doped Co featured fast reaction kinetics.[39] While in our Co-doped samples, the Co can not only improve the rate capability, but also help to activate the Li_2MnO_3 phase, therefore, a better rate performance was observed in samples with more Co. Note that the high rate performances of these samples after several activating cycles at low rate of 0.1 C were also measured; however, the results are not competitive to the traditional high-Co Li-rich cathode materials. For instance, the x=0.118 sample after 50 activation cycles at 0.1 C rate delivered a specific discharge capacity of ~ 170 mAh g^{-1} at 0.2 C rate and only ~ 110 mAh g^{-1} at 1 C rate. The capacity has subsequently dropped to ~100 mAh g^{-1} after 10 cycles at 1 C rate. To improve the rate performance, we are now investigating the reasons for poor rate performance and trying to improve it by surface modification methods, for instance, AlF_3 coating. The results will be reported in a future work.

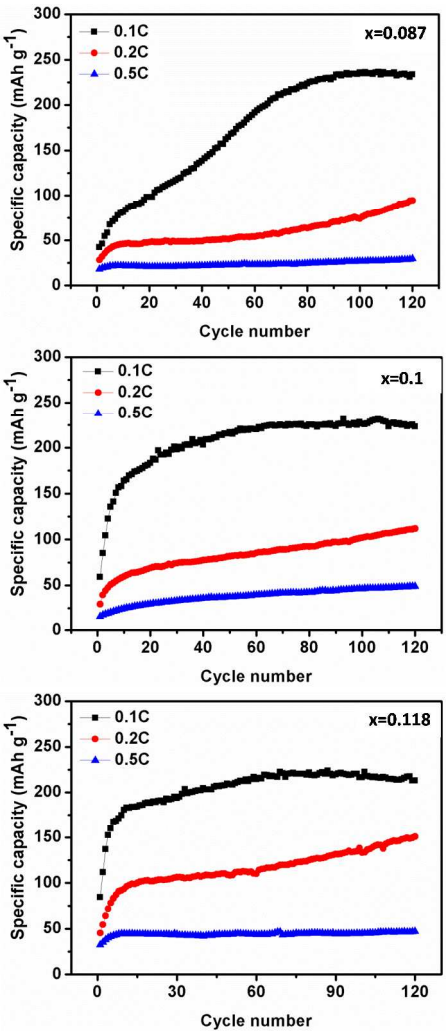

Figure 9. Cycling performance of the $Li[Co_xLi_{1/3-x/3}Mn_{2/3-2x/3}]O_2$ (x=0.087, 0.1, 0.118) composites at three current densities of 30, 60 and 150 mA g^{-1} between 2-4.8 V.

To investigate the kinetic properties of the Co-doped materials, EIS measurement was conducted on the assembled samples before and after 1 and 5 charging-discharging cycles at 2-4.8 V. The typical Nyquist plots and the corresponding equivalent circuit are shown in **Figure 10** and the fitting results based on this equivalent circuit are summarized in **Table S1**. Here R_1 is associated with the ohmic resistance between the working electrode and the reference electrode. In a general Nyquist plot, the high frequency intercept corresponds to the ohmic resistance of electrolyte solution and refers to R_2 in our model; the semicircle at medium frequency is related to the charge transfer resistance (R_3) on the electrode particle surface; and the sloping line at low frequency reflects the Li ion diffusion resistance in the crystal structure of the layered materials.[40] It can be found that the R_3 of all the samples decreased gradually during cycling. For example, from **Table 3**, R_3 of the x=0.1 sample reduced from 499 Ω to 221.7 Ω after the first cycle and further decreased to 193.2 Ω after 5 cycles, which is attributable to step-wise Li_2MnO_3 phase activation.[41, 42] On the other hand, after 1 or 5 cycles, it is found that the more the Co doping, the shorter the radius of the semicircle and

the lower the charge transfer resistance on the particle surface. For example, after 1st cycle, the values of R_3were 443.6 Ω, 221.7 Ω and 142.8 Ω for the x=0.087, 0.1 and 0.118 samples, respectively, and they further decreases to 305.1 Ω, 193.2 Ω and 169.1 Ω after 5 cycles. Therefore, it is reasonable to conclude that the faster decrease of R_3 in samples with higher Co doping is due to a faster activation rate of the Li_2MnO_3 phase. It worth noting that, to better understand the EIS results and the kinetic mechanism of the activation process, the use of a 3-electrode cell under protective atmosphere can be very useful in our future investigations.

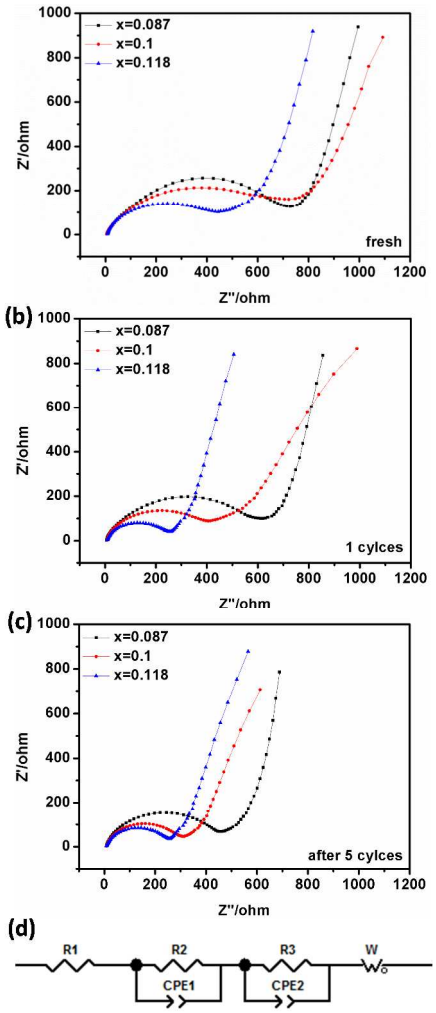

Figure 10. Typical Nyquist plots of the Co-doped samples (a) before and after (b) 1 and (c) 5 charging-discharging cycles.

The electrodes of Co-doped samples after 120 charging-discharging cycles at 0.1 C between 2-4.8 V were collected and characterized by *ex-situ* XRD (**Figure 11**). The C2/m featured minor peaks between 20° and 25° disappeared in all samples after 120 cycles of deep Li^+ intercalation/deintercalation, indicating the thorough consumption of the Li_2MnO_3 phase.[43] In addition, the XRD patterns of the cycled samples are very close to the $LiMnO_2$ (R-3m) structure, suggesting the structure evolution of the parent C2/m to the R-3m that could be induced by the irreversible 2b site Li^+ extraction to accommodate the crystal distortion.[19] Note that the phase transformation of Li_2MnO_3 during cycling has been a research focus.[43] During the activation process, it can be firstly transformed to a layered-like phase in the initial a few cycles during deep charging at high voltage, and the new phase could be further activated to provide the extra capacity in the following cycles.

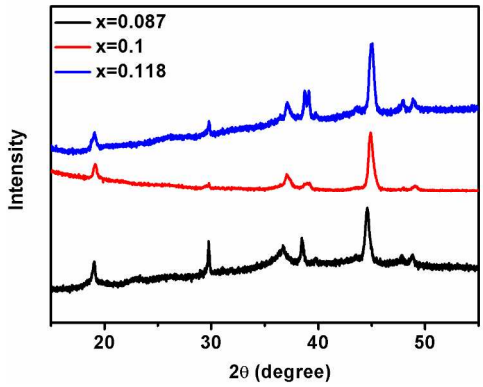

Figure 11. Ex-situ XRD patterns of the x=0.087, x=0.1 and x=0.118 electrodes after 120 charging-discharging cycles at 0.1C between 2-4.8 V.

Conclusions

A serial of low-Co Li-rich cathode materials $Li[Co_xLi_{1/3-x/3}Mn_{2/3-2x/3}]O_2$ (x=0.087, 0.1, 0.118) have been prepared by a simple co-precipitation method. Although these cathode materials showed similar crystal structure, morphology and microstructure, the low Co-doped ones exhibited prominent capacity increase gradually over tens of cycles which rarely occurred in the pure Li_2MnO_3 sample. This large stepwise capacity increase from less than 50 mAh g^{-1} in the first cycle to up to 250 mAh g^{-1} in a few dozens of cycles has been demonstrated as the result of the gradual activation of the Li_2MnO_3 phase which is promoted by the Co-doping.[18] The systematic study on this unique phenomenon of capacity increase revealed that the capacity increase was highly dependent on a few factors including the amount of Co-doping, cycling potential window and the current rate. All the low Co-doped samples can efficiently activate the Li_2MnO_3 phase and a minor change of the Co content can make a significant impact on the rate of the activation process. In addition, an appropriate cycling potential window of 2-4.8 V was proved to be effective in facilitating the Li_2MnO_3 activation and delivering excellent long-term cycling stability. These findings provide a deep understanding of the origin of superior high specific capacities of Li-rich cathode materials, which can be important to guide the rational design of cheap and high performance cathode materials for lithium ion batteries.

Acknowledgements

D.Y. acknowledges financial support from Chinese Scholarship Council (CSC) and authors are grateful to ARC through its LP and DP programs. The Australian Microscopy & Microanalysis Research Facility is acknowledged for providing characterization faculties.

Notes and references

[a] Nanomaterials Centre, School of Chemical Engineering and Australian Institute of Bioengineering and Nanotechnology, The University of Queensland Brisbane, QLD 4072, Australia, E-mail: l.wang@uq.edu.au,
[b] Materials Engineering, The University of Queensland, Brisbane, QLD 4072, Australia
[c] Centre for Microscopy and Microanalysis, The University of Queensland, Brisbane, QLD 4072, Australia

Electronic Supplementary Information (ESI) available: [details of any supplementary information available should be included here]. See DOI: 10.1039/b000000x/

1. B. Dunn, H. Kamath and J.-M. Tarascon, *Science*, 2011, **334**, 928-935.
2. M. Armand and J.-M. Tarascon, *Nature*, 2008, **451**, 652-657.
3. J. Liu, *Adv. Funct. Mater.*, 2013, **23**, 924-928.
4. H. Wang, L.-F. Cui, Y. Yang, H. Sanchez Casalongue, J. T. Robinson, Y. Liang, Y. Cui and H. Dai, *J. Am. Chem. Soc.*, 2010, **132**, 13978-13980.
5. B. Luo, B. Wang, M. Liang, J. Ning, X. Li and L. Zhi, *Adv. Mater.*, 2012, **24**, 1405-1409.
6. G. Jeong, J.-G. Kim, M.-S. Park, M. Seo, S. M. Hwang, Y.-U. Kim, Y.-J. Kim, J. H. Kim and S. X. Dou, *ACS nano*, 2014, **8**, 2977-2985.
7. C. K. Chan, R. N. Patel, M. J. O'Connell, B. A. Korgel and Y. Cui, *ACS Nano*, 2010, **4**, 1443-1450.
8. J. B. Goodenough and K.-S. Park, *J. Am. Chem. Soc.*, 2013, **135**, 1167-1176.
9. M. M. Thackeray, S.-H. Kang, C. S. Johnson, J. T. Vaughey, R. Benedek and S. Hackney, *J. Mater. Chem.*, 2007, **17**, 3112-3125.
10. M. M. Thackeray, C. S. Johnson, J. T. Vaughey, N. Li and S. A. Hackney, *J. Mater. Chem.*, 2005, **15**, 2257-2267.
11. A. R. Armstrong, M. Holzapfel, P. Novák, C. S. Johnson, S.-H. Kang, M. M. Thackeray and P. G. Bruce, *J. Am. Chem. Soc.*, 2006, **128**, 8694-8698.
12. H. Yu, R. Ishikawa, Y. G. So, N. Shibata, T. Kudo, H. Zhou and Y. Ikuhara, *Angew. Chem., Int. Ed.*, 2013, **52**, 5969-5973.
13. H. Yu and H. Zhou, *J. Phys. Chem. Lett.*, 2013, **4**, 1268-1280.
14. K. A. Jarvis, C. C. Wang, A. Manthiram and P. J. Ferreira, *J. Mater. Chem. A*, 2014, **2**, 1353-1362.
15. Y. J. Park, Y.-S. Hong, X. Wu, M. G. Kim, K. S. Ryu and S. H. Chang, *J. Electrochem. Soc.*, 2004, **151**, A720-A727.
16. J.-M. Kim, S. Tsuruta and N. Kumagai, *Electrochem. Commun.*, 2007, **9**, 103-108.
17. N. Kumagai, J. M. Kim, S. Tsuruta, Y. Kadoma and K. Ui, *Electrochim. Acta*, 2008, **53**, 5287-5293.
18. D. Ye, K. Ozawa, B. Wang, D. Hulicova-Jurcakova, J. Zou, C. Sun and L. Wang, *Nano Energy*, 2014, **6**, 92-102.
19. K. Ozawa, Y. Nakao, T. Mochiku, Z. Cheng, L. Wang, H. Iwai, Y. Tsuchiya, H. Fujii and N. Igawa, *J. Electrochem. Soc.*, 2012, **159**, A300-A304.
20. S.-H. Kang, P. Kempgens, S. Greenbaum, A. Kropf, K. Amine and M. Thackeray, *J. Mater. Chem.*, 2007, **17**, 2069-2077.
21. J. Bréger, M. Jiang, N. Dupré, Y. S. Meng, Y. Shao-Horn, G. Ceder and C. P. Grey, *J. Solid State Chem.*, 2005, **178**, 2575-2585.
22. K. A. Jarvis, Z. Deng, L. F. Allard, A. Manthiram and P. J. Ferreira, *Chem. Mater.*, 2011, 23, 3614-3621.
23. Y. Li, Z. Zhou, M. Ren, X. Gao and J. Yan, *Electrochim. Acta*, 2006, 51, 6498-6502.
24. L. Zhou, D. Zhao and X. D. Lou, *Angew. Chem.*, 2012, 124, 243-245.
25. Y. Jiang, Z. Yang, W. Luo, X. Hu and Y. Huang, *Phys. Chem. Chem. Phys.*, 2013, 15, 2954-2960.
26. J. Bareno, C. Lei, J. Wen, S. H. Kang, I. Petrov and D. Abraham, *Adv. Mater.*, 2010, **22**, 1122-1127.
27. A. Boulineau, L. Croguennec, C. Delmas and F. Weill, *Chem. Mater.*, 2009, **21**, 4216-4222.
28. E. Regan, T. Groutso, J. Metson, R. Steiner, B. Ammundsen, D. Hassell and P. Pickering, *Surf. Interface Anal.*, 1999, **27**, 1064-1068.
29. Z. Li, J. Wang, S. Liu, X. Liu and S. Yang, *J. Power Sources*, 2011, **196**, 8160-8165.
30. S. Madhavi, G. S. Rao, B. Chowdari and S. Li, *J. Electrochem. Soc.*, 2001, **148**, A1279-A1286.
31. A. van Bommel, L. Krause and J. Dahn, *J. Electrochem. Soc.*, 2011, **158**, A731-A735.
32. A. Ito, D. Li, Y. Sato, M. Arao, M. Watanabe, M. Hatano, H. Horie and Y. Ohsawa, *J. Power Sources*, 2010, **195**, 567-573.
33. K. T. Lee, S. Jeong and J. Cho, *Acc. Chem. Res.*, 2012, **46**, 1161-1170.
34. N. Yabuuchi, K. Yoshii, S.-T. Myung, I. Nakai and S. Komaba, *J. Am. Chem. Soc.*, 2011, **133**, 4404-4419.
35. B. Xu, C. R. Fell, M. Chi and Y. S. Meng, *Energy Environ. Sci.*, 2011, **4**, 2223-2233.
36. M. Gu, I. Belharouak, J. Zheng, H. Wu, J. Xiao, A. Genc, K. Amine, S. Thevuthasan, D. R. Baer and J. G. Zhang, *Acs Nano*, 2012, **7**, 760-767.
37. B. Song, Z. Liu, M. O. Lai and L. Lu, *Phys. Chem. Chem. Phys.*, 2012, **14**, 12875-12883.
38. J. R. Croy, D. Kim, M. Balasubramanian, K. Gallagher, S.-H. Kang and M. M. Thackeray, *J. Electrochem. Soc.*, 2012, **159**, A781-A790.
39. X. Yu, Y. Lyu, L. Gu, H. Wu, S. M. Bak, Y. Zhou, K. Amine, S. N. Ehrlich, H. Li and K. W. Nam, *Adv. Energy Mater.*, 2013.
40. O. Toprakci, H. A. Toprakci, Y. Li, L. Ji, L. Xue, H. Lee, S. Zhang and X. Zhang, *J. Power Sources*, 2013, **241**, 522-528.
41. K. Du, F. Yang, G. R. Hu, Z. D. Peng, Y. B. Cao and K. S. Ryu, *J. Power Sources*, 2013, **244**, 29-34.
42. X. Dong, Y. Xu, L. Xiong, X. Sun and Z. Zhang, *J. Power Sources*, 2013, **243**, 78-87.
43. E.-S. Lee, A. Huq, H.-Y. Chang and A. Manthiram, *Chem. Mater.*, 2012, **24**, 600-612.

